Polarimetric Full-Wavefield Coherent Lidar

DONGYU DU,[1,2,*] ANDREW XIE,[1,2] PARSA MIRDEHGHAN,[1,2] BRANDON BUSCAINO,[3] SEUNG-HWAN BAEK,[4], KIRIAKOS N. KUTULAKOS,[1,2] DAVID B. LINDELL,[1,2]

[1] *Computer Science Department, University of Toronto, Toronto, Ontario, Canada*
[2] *Vector Institute, Toronto, Ontario, Canada*
[3] *Ciena Corporation, San Jose, California, US*
[4] *Department of Computer Science and Engineering, Pohang University of Science and Technology (POSTECH), Pohang, Gyeongsangbuk-do, Republic of Korea*
[*] *dongyu@cs.toronto.edu*

Abstract: Coherent lidar recovers a scene's geometry and motion by measuring the time-of-flight and Doppler shift of backscattered light. However, conventional coherent lidar systems do not capture the full optical wavefield—comprising time-varying amplitude, phase, and polarization—and therefore forfeit access to an additional, rich source of scene information: surface material properties encoded in the polarization state of backscattered light and in the statistical properties of coherent polarization speckle. Prior approaches to full-wavefield sensing require complex benchtop optics for ultrafast modulation and detection, or do not address the modeling and recovery of the surface polarimetric response, which is scrambled by inter-reflections within the lidar's internal optics. Here, we introduce a polarimetric full-wavefield coherent lidar system that recovers a surface point's Jones matrix—encoding material and geometric surface properties as observed through the system's illumination and collection aperture—along with depth and velocity, all from a single measurement. We achieve this by (1) repurposing an off-the-shelf coherent optical modem—conventionally used for telecommunications—for ultrafast full-wavefield modulation and detection, and (2) developing a novel, polarization-aware image formation model and inverse method that disentangles the system's optical response from that of a target surface. Overall, the approach delivers millimeter-accurate depth, robust velocimetry, and polarimetric surface properties, all with microsecond-scale exposures, eye-safe optical power, and insensitivity to ambient light.

1. Introduction

Coherent lidar systems illuminate a scene with a modulated light source and interfere the backscattered signal with a local oscillator to recover range and velocity. Compared to incoherent lidar, coherent detection achieves shot-noise–limited sensitivity through coherent mixing gain [1] and directly measures velocity via Doppler frequency shifts [2], making it widely used in atmospheric sensing [3, 4], robotic navigation [5], and long-range remote sensing [6].

In principle, coherent detection provides access to the full optical wavefield—amplitude, phase, and polarization—which encodes not only range and velocity but also material-related properties and micro-scale surface structure through the scene's coherent polarimetric response (i.e., the Jones matrix [7]) and the statistics of polarization speckle [8]. This full-wavefield information could extend lidar beyond sensing geometry and motion to enable physical scene understanding, which is important in autonomous driving [9–11], robotic manipulation [12–16] and maritime sensing [17–20]. In practice, however, existing lidar systems do not fully exploit the full optical wavefield due to challenges related to measurement acquisition and computational modeling.

The first challenge is acquiring full-wavefield measurements. Existing coherent lidar architectures either acquire only a subset of the wavefield or require complex custom optical setups. Standard frequency-modulated continuous-wave (FMCW) systems [21, 22] measure amplitude and phase only in a single polarization channel; polarimetric FMCW variants [23] extend this to

multiple polarization states but demand additional beam synchronization optics and specialized optical hardware. Random-modulated continuous-wave (RMCW) systems [24–26] typically rely on either amplitude or phase modulation, but achieving millimeter-scale range resolution requires ultrafast modulation at rates exceeding tens of gigahertz, which remains difficult to realize in practice. Thus, neither architecture achieves a practical measurement front end for acquiring the polarimetric full-wavefield response of the scene.

The second challenge is how to computationally model full-wavefield lidar measurements. Even when coherent polarization information is available, existing systems lack the computational framework to exploit it in the context of lidar. For example, coherent polarimetric sensing has been demonstrated in adjacent modalities such as optical coherence tomography [27–29], but extending these ideas to lidar requires sophisticated inverse modeling that accounts for Doppler shifts, phase noise, speckle statistics, polarization-dependent scattering, and inter-reflections within the system's own optics.

Recently, Mirdehghan et al. [30] addressed the measurement acquisition challenge by repurposing a coherent optical modem—a device commonly used for high-bandwidth optical communications [31]—for lidar sensing. Optical modems provide a nearly off-the-shelf platform for ultrafast (>70 GHz) random amplitude and phase modulation in multiple polarization channels, along with coherent detection of the full optical wavefield. Adapting one for lidar requires only modest hardware changes: routing the output and input ports through a circulator and coupling to free space through a collimator. Yet, despite these full-wavefield sensing capabilities, the approach of Mirdehghan et al. does not recover the polarimetric response of a measured surface. A key challenge is that the transmitted and received waveforms interact with optical surfaces inside the lidar, coupling the system's own polarization response with that of the scene. Disentangling the two requires both a polarization-aware image formation model that accounts for these internal interactions and a calibration procedure to characterize the system's Jones matrices.

Here, we repurpose a compact, off-the-shelf coherent optical modem to realize a full-wavefield coherent lidar system with polarimetric sensing as shown in Fig. 1(a). The modem's modulation scheme is most closely related to RMCW lidar, but with the distinction that modulation is applied jointly to both amplitude and phase across two orthogonal polarization states, enabling full-wavefield sensing. Central to our approach is a polarization-aware image formation model and inverse algorithm that separates the scene-dependent effective backscattering Jones response from polarization distortions introduced by internal optical interfaces. We implement the approach through a system calibration procedure and per-pixel offline optimization. We also show that we can measure polarimetric speckle—whose properties correlate with micro-scale surface roughness—and that we can infer material-related properties from the spatial degree of polarization of the reflected field. Finally, we demonstrate using the polarimetric response to distinguish between materials observed through a scattering layer. Overall, our approach yields millimeter-accurate depth, robust velocimetry, and polarimetric surface characterization, as shown in Fig. 1, all with microsecond-scale exposures, eye-safe optical power, and insensitivity to ambient illumination.

2. Polarimetric Coherent Measurement Model

We present a model of the coherent modulation and detection process implemented by the optical modem, and we analyze the effects introduced by partial polarization of backscattered light. The coherent lidar system modulates both the amplitude and phase of light in two orthogonal linear polarization channels. As illustrated in Fig. 1(a), this modulated wavefront is transmitted through a fiber collimator, scanner, and circulator to illuminate the scene. After interacting with a surface, the backscattered field is coupled back into the fiber, routed by the circulator to the modem and recovered via homodyne detection in each channel. The returned signal consists of a component

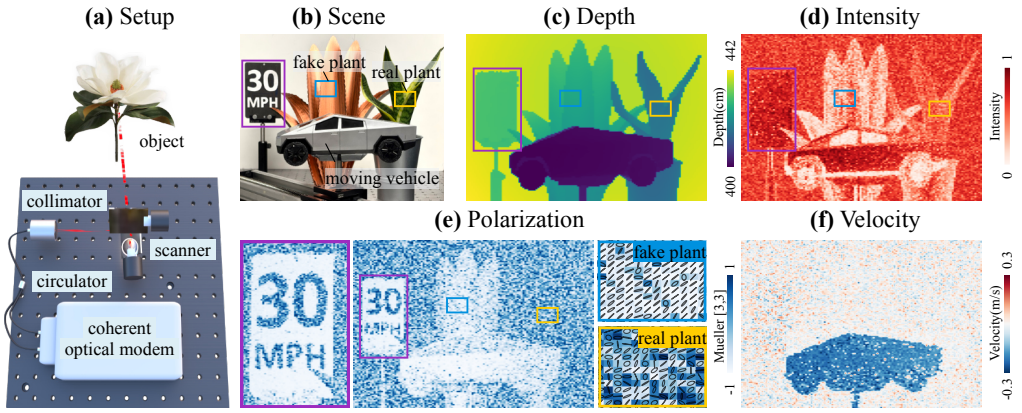

Fig. 1. **Simultaneous ranging, velocimetry, and polarimetric sensing with polarimetric full-wavefield coherent lidar.** **(a)** Experimental setup based on an off-the-shelf coherent optical modem, fiber collimator, circulator, and scanning mirrors for dual-polarization coherent measurement. **(b)** Experimental scene containing a moving model vehicle, a speed-limit sign, an artificial plant, and a real plant, mimicking a simplified road-side environment with both static and dynamic objects. **(c)** Reconstructed depth map, which localizes the spatial layout of the vehicle, sign, and surrounding vegetation. **(d)** Reconstructed intensity map, where the sign lettering is not resolved because the sign has nearly uniform albedo at the modem wavelength of 1550 nm. **(e)** Reconstructed polarization map, visualized by the Mueller M_{33} component and local polarization ellipses. The polarization map reveals material-sensitive details that are not resolved by depth or intensity, including the sign text and the difference between artificial and real vegetation. **(f)** Reconstructed Doppler velocity map, which identifies the moving vehicle and separates it from the static background.

that can be described by a Jones matrix, as well as a randomly polarized component that couples into the coherent detection process and gives rise to speckle. We provide an overview of this model in Fig. 2.

2.1. Modulation and Detection

Modulation. A narrow-linewidth continuous-wave laser provides the optical carrier at frequency f_0. The coherent optical modem generates two known complex baseband waveforms in the orthogonal X and Y polarization channels. Specifically, the carrier is split into two polarization branches using a polarization beam splitter, and each branch is independently modulated by the modem-controlled dual-drive Mach–Zehnder modulators. The electrical symbol streams applied to the modulators control both the instantaneous amplitude and phase of each optical field component, producing the complex baseband signals $s_X(t) = A_X(t)e^{j\phi_X(t)}$ and $s_Y(t) = A_Y(t)e^{j\phi_Y(t)}$. Here, $A_X(t)$ and $A_Y(t)$ denote the time-varying field-envelope amplitudes, and $\phi_X(t)$ and $\phi_Y(t)$ denote the corresponding phase modulation waveforms in the two linear polarization channels. The two components are subsequently recombined to form $\mathbf{E}_{\mathrm{tx}}(t)$, the transmitted dual-polarization optical field, which can be expressed as:

$$\mathbf{E}_{\mathrm{tx}}(t) = \begin{bmatrix} A_X(t)e^{j\phi_X(t)} \\ A_Y(t)e^{j\phi_Y(t)} \end{bmatrix} e^{j2\pi f_0 t} = \mathbf{s}(t)\, e^{j2\pi f_0 t}, \tag{1}$$

where $\mathbf{s}(t) = [s_X(t), s_Y(t)]^T$ is the known dual-polarization complex baseband waveform generated by the optical modem and used as the probing signal in our forward model. Because

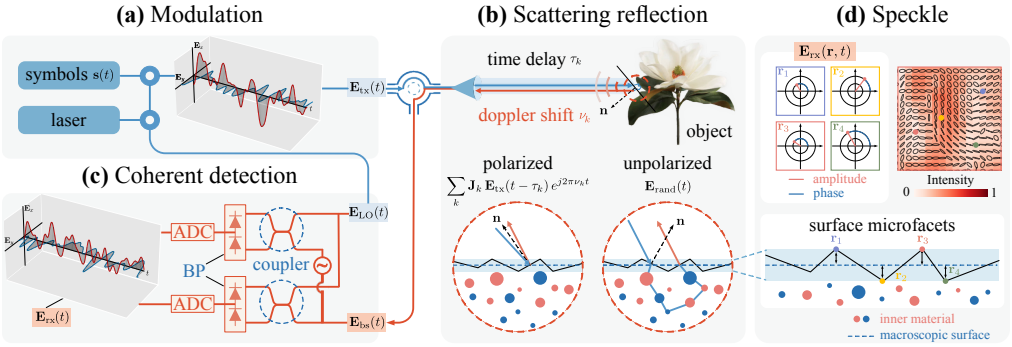

Fig. 2. **Polarimetric coherent measurement model.** **(a)** The baseband waveform $\mathbf{s}(t)$ modulates the laser to synthesize a dual-polarization optical field $\mathbf{E}_{\text{tx}}(t)$. **(b)** The received field is a superposition of time-delayed (τ_k) and Doppler-shifted (ν_k) polarized echoes, together with a randomly polarized component $\mathbf{E}_{\text{rand}}(t)$ arising from multiple scattering. **(c)** The returned signal $\mathbf{E}_{\text{bs}}(t)$ interferes with a local oscillator $\mathbf{E}_{\text{LO}}(t)$ in a balanced receiver; bandpass filtering and analog-to-digital (ADC) sampling yield complex baseband measurements $\mathbf{E}_{\text{rx}}(t)$ in two polarization channels. **(d)** The measured field $\mathbf{E}_{\text{rx}}(\mathbf{r}, t)$ varies across spatial locations $\mathbf{r}$ due to coherent interference among surface microfacets, resulting in intensity and polarization speckle.

both polarization channels are independently modulated in amplitude and phase, $\mathbf{s}(t)$ provides a time-varying set of input polarization states for estimating the polarimetric scene response.

Free-space coupling and surface backscattering. After modulation, $\mathbf{E}_{\text{tx}}(t)$ is transmitted through a single-mode fiber, an amplifier, and an optical circulator (see Fig. 2) before being collimated into free space. Then, the backscattered light from the scene is subsequently recollected by the same collimator and routed through the circulator to the receiver port of the optical modem. We model the received waveform by accounting for (1) round-trip propagation delays from internal and scene reflections, (2) polarization changes induced by the fiber, internal optics, and scene surface, (3) Doppler-induced carrier-frequency shifts, and (4) a random, unpolarized field generated by surface scattering. The backscattered field $\mathbf{E}_{\text{bs}}(t)$ is thus written as:

$$\mathbf{E}_{\text{bs}}(t) = \sum_k \mathbf{J}_k \, \mathbf{E}_{\text{tx}}(t - \tau_k) \, e^{j2\pi\nu_k t} + \mathbf{E}_{\text{rand}}(t). \tag{2}$$

Here, $\mathbf{J}_k$ is the Jones matrix corresponding to the k-th surface reflection, which models a deterministic polarization transformation; τ_k and ν_k represent the corresponding time delay and Doppler frequency shift; and $\mathbf{E}_{\text{rand}}(t)$ is a random, unpolarized component of the optical field that cannot be represented by a single Jones matrix transformation.

Coherent detection. The backscattered field $\mathbf{E}_{\text{bs}}(t)$ is routed by the circulator to the coherent receiver of the optical modem. Inside the modem receiver, the returned signal is combined with a strong local-oscillator (LO) field $\mathbf{E}_{\text{LO}}(t)$ using an optical hybrid. For each polarization channel, the hybrid produces in-phase and quadrature interference outputs, which are measured by balanced photodetectors and digitized to form the complex baseband samples. Under the strong-LO approximation [32], the differential photocurrent is proportional to the interference term between the LO and the received optical field, yielding

$$\mathbf{E}_{\text{rx}}(t) = \kappa \, \mathbf{E}_{\text{LO}}^{\dagger}(t) \left(\sum_k \mathbf{J}_k \, \mathbf{E}_{\text{tx}}(t - \tau_k) \, e^{j2\pi\nu_k t} + \mathbf{E}_{\text{rand}}(t) \right) + \boldsymbol{\eta}(t), \tag{3}$$

where $(\cdot)^\dagger$ denotes the Hermitian transpose, κ is the heterodyne mixing constant [33, 34], and $\boldsymbol{\eta}(t)$ denotes additive electronic and shot noise.

2.2. Coherency and Polarization Speckle

Up to this point, we have modeled the received electric field, $\mathbf{E}_{\text{rx}}$, as the sum of a coherent component described by interaction with the Jones matrices $\mathbf{J}_k$ and random components captured by $\mathbf{E}_{\text{rand}}$ and $\boldsymbol{\eta}(t)$. We now describe how to use the coherency matrix [7] to model the fraction of randomly polarized light in $\mathbf{E}_{\text{rx}}$, and we explain how the coherent interactions of light give rise to polarization speckle.

Coherency matrix. To analyze the polarization characteristics of $\mathbf{E}_{\text{rx}}$, we analyze its second-order coherence through the coherency matrix: $\mathbf{C}_{\text{out}} = \mathbb{E}\Big[\mathbf{E}_{\text{rx}}(t)\mathbf{E}_{\text{rx}}^\dagger(t)\Big]$, where $\mathbb{E}[\cdot]$ denotes time averaging. $\mathbf{C}_{\text{out}}$ is a 2×2 Hermitian positive-semidefinite matrix that describes the amplitude and phase correlations between orthogonal polarization components. A statistical representation of polarized light can then be obtained by the eigen decomposition of $\mathbf{C}_{\text{out}}$:

$$\mathbf{C}_{\text{out}} = \lambda_1 \mathbf{v}_1 \mathbf{v}_1^\dagger + \lambda_2 \mathbf{v}_2 \mathbf{v}_2^\dagger, \quad \lambda_1 \geq \lambda_2 \geq 0, \tag{4}$$

where $\lambda_{1/2}$ and $\mathbf{v}_{1/2}$ are the eigenvalues and eigenvectors of $\mathbf{C}_{\text{out}}$. In Section 3, we introduce a statistical optimization model for estimating the fully polarized Jones term $\mathbf{J}_k$ and the incoherent power which is proportional to the unpolarized component λ_2.

Polarization speckle. In practice, coherent lidar measurements exhibit speckle because micron-scale variations in surface geometry create differing optical path lengths in the backscattered light [8].

We can describe this phenomenon by modeling the received field at detector position $\mathbf{r}$ and time t, which we denote $\mathbf{E}_{\text{rx}}(\mathbf{r}, t)$. This field is the coherent superposition of contributions from many micro-facets over the illuminated surface area $\mathcal{A}$:

$$\mathbf{E}_{\text{rx}}(\mathbf{r}, t) = \int_{\mathcal{A}} \mathbf{J}(\mathbf{r}')\, \mathbf{E}_{\text{tx}}(\mathbf{r}', t)\, e^{jk_0\left(|\mathbf{r}-\mathbf{r}'|+h(\mathbf{r}')\right)}\, \mathrm{d}\mathbf{r}' + \mathbf{E}_{\text{rand}}(\mathbf{r}, t). \tag{5}$$

Here, $\mathbf{J}(\mathbf{r}')$ denotes the local Jones matrix at surface point $\mathbf{r}'$, $h(\mathbf{r}')$ represents the micron-scale surface height profile, and k_0 is the optical wavenumber. The phase term encodes path-length variations caused by changes in surface height (Fig. 2(d)); increasing roughness (surface height variance) causes phase decorrelation between micro-facets, which in turn reduces the spatial degree of polarization and yields increasingly randomized polarization speckle.

3. Scene Reconstruction

We first introduce a statistical optimization model that jointly estimates Jones responses and incoherent power from the received field $\mathbf{E}_{\text{rx}}(t)$. Then, we show how to derive the depth and velocity based on the estimated Jones responses. Finally, we decompose the recovered Jones matrix into separate components that model the surface reflection, internal reflections and dispersion effects within the lidar system.

Statistical optimization model. Eq. (3) shows that the received coherent field $\mathbf{E}_{\text{rx}}(t)$ consists of a deterministic component induced by the modulated RMCW transmitted waveform, a random scattering component and additive receiver noise. Therefore, the measurement follows a complex Gaussian process: $\mathbf{E}_{\text{rx}}(t) \sim \mathcal{CN}\big(\boldsymbol{\mu}(t), \boldsymbol{\Sigma}(t)\big)$, as shown in Fig. 3(a). The mean value $\boldsymbol{\mu}(t)$ and covariance $\boldsymbol{\Sigma}(t)$ can be expressed as follows:

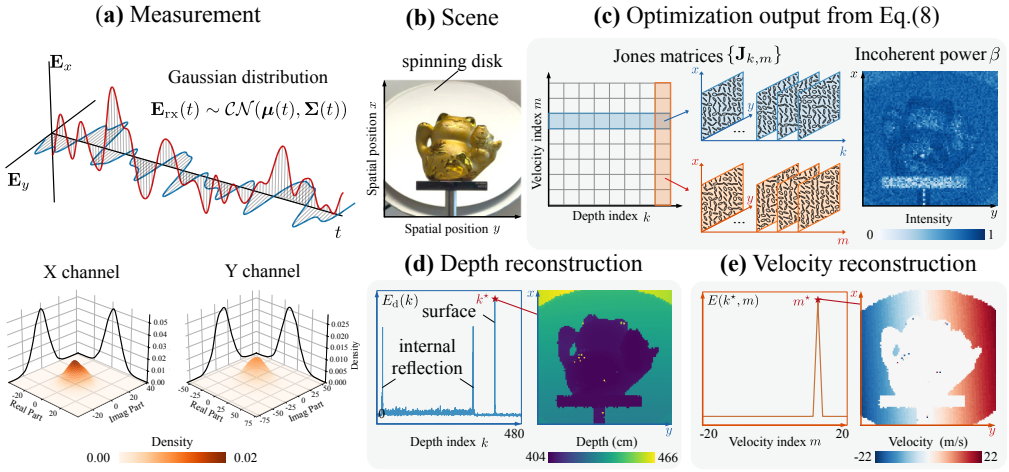

Fig. 3. **Scene reconstruction overview.** **(a)** The two-channel measurement $\mathbf{E}_{\mathrm{rx}}(t)$ is modeled as a complex Gaussian random process; the bottom plots show the empirical complex-Gaussian densities of the X and Y polarization channels. **(b)** Example scene capture (a spinning disk and a figurine) scanned over spatial coordinates (x, y). **(c)** We estimate per-pixel, depth–Doppler-indexed Jones matrices $\{\mathbf{J}_{k,m}\}$ together with an incoherent power β by minimizing the negative log-likelihood in Eq. (8). **(d)** We compute the measurement energy using the Frobenius norm of the Jones matrix, $E(k,m) = |\mathbf{J}_{k,m}|_F^2$, integrate over Doppler to obtain the depth profile $E_{\mathrm{d}}(k)$, and estimate depth as $k^\star = \arg\max_k E_{\mathrm{d}}(k)$. **(e)** We obtain velocity by identifying the dominant Doppler index $m^\star = \arg\max_m E(k^\star, m)$.

$$\boldsymbol{\mu}(t) = \kappa \mathbf{E}_{\mathrm{LO}}^{\dagger}(t) \sum_k \mathbf{J}_k \mathbf{E}_{\mathrm{tx}}(t-\tau_k) e^{j2\pi\nu_k t}, \qquad \boldsymbol{\Sigma}(t) = \big(\sigma_{\mathrm{het}}^2(t) + \beta(t)\big)\mathbf{I}_2. \tag{6}$$

The value $\sigma_{\mathrm{het}}(t)$ denotes the heterodyne noise variance [31], $\beta(t) = |\kappa|^2 \|\mathbf{E}_{\mathrm{LO}}\|^2 \lambda_2(t)$ corresponds to the incoherent power of the measured field, and $\lambda_2(t)$ is the second eigenvalue of the local coherency matrix in Eq. (4). A derivation of Eq. (6) is provided in Supplement 1, Section 1.A.

Directly optimizing the continuous Doppler shifts $\{\nu_k\}$ jointly with the Jones kernels $\{\mathbf{J}_k\}$ and the incoherent power term $\beta(t)$ leads to a highly non-convex problem. To obtain a stable and efficient solver, we discretize the Doppler axis onto a fixed grid $\{\nu_m\}_{m=1}^M$ and estimate a depth–velocity Jones response volume $\{\mathbf{J}_{k,m}\}$, as shown in Fig. 3(c). Accounting for this discretization, the mean value in Eq. (6) becomes

$$\boldsymbol{\mu}(t) = \kappa\, \mathbf{E}_{\mathrm{LO}}^{\dagger}(t) \sum_k \sum_{m=1}^{M} \mathbf{J}_{k,m}\, \mathbf{E}_{\mathrm{tx}}(t-\tau_k)\, e^{j2\pi\nu_m t}. \tag{7}$$

Assuming independent samples in time, we estimate the depth–velocity Jones response volume, and the incoherent power term by minimizing the negative log-likelihood of the corresponding Gaussian distribution. Additionally, we introduce a sparsity-promoting regularization term to stabilize the ill-posed inversion and suppress spurious depth and velocity responses. The resulting objective function is given as

$$\min_{\{\mathbf{J}_{k,m}\},\beta} \sum_t \left(2\log q + \frac{\big\|\mathbf{E}_{\mathrm{rx}}(t) - \boldsymbol{\mu}(t)\big\|_2^2}{q} \right) + \lambda_{\mathrm{reg}} \sum_{k,m} \big\|\mathbf{J}_{k,m}\big\|_F, \tag{8}$$

where $\|\cdot\|_F$ denotes the Frobenius norm of the Jones matrix, λ_{reg} controls the strength of the regularization, and q is the variance term in the diagonal covariance $\mathbf{\Sigma}(t)$. A stability analysis of this scalar-covariance approximation under anisotropic depolarized covariance and polarization-dependent noise is provided in Supplement 1, Section 1.D. Over each acquisition window, we assume approximately stationary noise statistics and therefore adopt a time-invariant variance $q = \sigma_{\text{het}}^2 + \beta$. Here σ_{het}^2 is obtained via a noise-floor estimation from a measurement window without target returns (see details in Supplement 1, Section 1.B), and $\beta \geq 0$ captures the additional variance induced by the incoherent power.

Depth and velocity estimation. To recover depth and Doppler, we convert the estimated depth–velocity Jones response volume $\{\mathbf{J}_{k,m}\}$ to an energy map by computing the Frobenius norm of the Jones matrices: $E(k,m) = \|\mathbf{J}_{k,m}\|_F^2$. We then integrate over the Doppler bins to form a 1D depth profile $E_{\text{d}}(k)$ and pick the target delay index as the strongest return, $k^\star = \arg\max_k E_{\text{d}}(k)$. Given the selected depth $k^\star$, we estimate the Doppler index from the corresponding velocity profile by $m^\star = \arg\max_m E(k^\star, m)$, yielding the final depth and velocity estimates $\tau_{k^\star}$ and $v_{m^\star}$. Repeating this procedure over all spatially scanned pixels produces the depth map and velocity map shown in Fig. 3(d–e).

Decomposing the surface-reflection Jones matrix. The depth–velocity index $(k^\star, m^\star)$ identifies the Jones matrix $\mathbf{J}^\star \triangleq \mathbf{J}_{k^\star,m^\star}$, which represents the combined round-trip polarization response of the system, including the transmit-path optics $\mathbf{J}_{\text{tx}}$, the surface reflection $\mathbf{J}_{\text{surf}}$, and the receive-path optics $\mathbf{J}_{\text{rx}}$. To recover the surface polarization, we separately model the response of the transmitted and received optical paths and computationally remove their effects. Once $\mathbf{J}_{\text{tx}}$ and $\mathbf{J}_{\text{rx}}$ are calibrated (described in Section 4), the decoupled surface Jones matrix is obtained as:

$$\mathbf{J}_{\text{surf}} = \gamma^{-1}\, \mathbf{J}_{\text{rx}}^{-1}\, \mathbf{J}^\star\, \mathbf{J}_{\text{tx}}^{-1}. \tag{9}$$

where $\gamma \in \mathbb{R}_+$ denotes a global amplitude gain.

$\mathbf{J}_{\text{surf}}$ is an effective backscattering Jones response observed through the system's illumination and collection aperture. We analyze its effective polarimetric descriptors—including diattenuation and retardance—using the standard polar decomposition [35]. These parameters provide physically interpretable cues for material discrimination and surface characterization. Beyond per-pixel properties, $\mathbf{J}_{\text{surf}}$ also exhibits rich spatial variations driven by micro-geometry and coherent interference, which manifest as polarization speckle patterns across the scanned field of view. We analyze the spatial structure of polarization speckle using the spatial degree of polarization (SDoP) [8, 36], which we show is useful to compare materials and surface roughness. We provide precise definitions of these quantities (diattenuation, retardance, and SDoP) in Supplement 1, Section 1.C. We further analyze the stability of the joint depth–velocity–Jones reconstruction under random initialization in Supplement 1, Section 1.F.

4. Polarimetric Calibration

As illustrated in Fig. 4(a), the polarization state measured by the coherent receiver is shaped not only by the scene, but also by polarization distortions accumulated along the transmitted and received optical paths, including the fiber link, erbium-doped fiber amplifier (EDFA), circulator, collimator and scanner. We abstract these path-dependent distortions as two Jones operators, $\mathbf{J}_{\text{tx}}$ and $\mathbf{J}_{\text{rx}}$, which compactly represent the cascaded polarization transformations of the transmitted and received paths, respectively. Accordingly, we design a calibration setup and an end-to-end optimization procedure to jointly estimate $\mathbf{J}_{\text{tx}}$ and $\mathbf{J}_{\text{rx}}$ from a set of captured measurements.

First, we insert a rotating linear polarizer in the common transmitted/received path to generate controllable polarization states at the target and thereby obtain multiple linearly independent

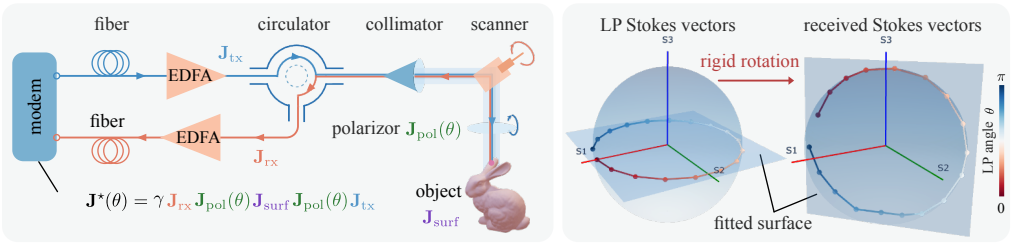

Fig. 4. **Polarimetric calibration overview.** **(a)** A rotating linear polarizer with Jones operator $\mathbf{J}_{\mathrm{pol}}(\theta)$ is inserted in the common transmitted/received path to generate known polarization states. The measured response is modeled as $\mathbf{J}^{\star}(\theta) = \gamma \mathbf{J}_{\mathrm{rx}} \mathbf{J}_{\mathrm{pol}}(\theta) \mathbf{J}_{\mathrm{surf}} \mathbf{J}_{\mathrm{pol}}^{\dagger}(\theta) \mathbf{J}_{\mathrm{tx}}$, where $\mathbf{J}_{\mathrm{tx}}$ and $\mathbf{J}_{\mathrm{rx}}$ represent the polarization distortions introduced by the transmitted and received optical paths of the optical train (fiber, EDFA, circulator, collimator and scanner), respectively. $\mathbf{J}_{\mathrm{surf}}$ is the Jones matrix of the calibration object. **(b)** As θ varies, the Stokes vectors of the linear polarization (LP) states trace a circle on the Poincaré sphere; after propagation through the system, the Stokes vectors remain on a rotated circle, consistent with a unitary polarization transformation.

measurements during calibration. Note that the polarizer is used only during calibration and removed for all subsequent imaging experiments. For a polarizer angle θ, the estimated combined surface response $\mathbf{J}(\theta)$ is

$$\mathbf{J}(\theta) = \gamma \mathbf{J}_{\mathrm{rx}} \mathbf{J}_{\mathrm{pol}}(\theta) \mathbf{J}_{\mathrm{surf}} \mathbf{J}_{\mathrm{pol}}^{\dagger}(\theta) \mathbf{J}_{\mathrm{tx}}. \tag{10}$$

We define $\mathbf{J}_{\mathrm{pol}}(\theta)$ to be the Jones operator of a linear polarizer at angle θ [37]:

$$\mathbf{J}_{\mathrm{pol}}(\theta) = \mathbf{R}(\theta)\, \mathbf{P}_0\, \mathbf{R}^{\mathsf{T}}(\theta), \quad \mathbf{R}(\theta) = \begin{bmatrix} \cos\theta & -\sin\theta \\ \sin\theta & \cos\theta \end{bmatrix}, \quad \mathbf{P}_0 = \begin{bmatrix} 1 & 0 \\ 0 & 0 \end{bmatrix}. \tag{11}$$

The matrix $\mathbf{R}(\theta)$ denotes a rotation operator that aligns the linear polarizer's transmission axis with the measurement coordinate frame, and $\mathbf{P}_0$ represents an ideal horizontal linear polarizer. For the calibration target we assume a homogeneous, non-depolarizing planar surface whose Jones matrix can be diagonalized in its principal polarization basis, so we parameterize it as the rotated diagonal form:

$$\mathbf{J}_{\mathrm{surf}} = \mathbf{R}(\alpha)^{\mathsf{T}} \begin{bmatrix} r_1 e^{j\phi_1} & 0 \\ 0 & r_2 e^{j\phi_2} \end{bmatrix} \mathbf{R}(\alpha), \tag{12}$$

with amplitude–phase coefficients (r_1, ϕ_1) and (r_2, ϕ_2) in the principal axes and an in-plane orientation α.

Unitary approximation. Polarization evolution in single-mode fibers and reciprocal passive optics can be approximated by a unitary Jones operator [38]. Geometrically, a unitary Jones transformation corresponds to a rigid rotation on the Poincaré sphere; thus, the locus traced by a rotating linear polarizer forms an equatorial circle that remains invariant under the transformation. Our experimental observations in Fig. 4(b) further confirm this assumption (see Supplement 1, Section 2.A for a derivation and details). We therefore parameterize $\mathbf{J}_{\mathrm{tx}}$ and $\mathbf{J}_{\mathrm{rx}}$ as a rotation

followed by a linear retarder:

$$\mathbf{U}(\psi,\delta,\vartheta) = \mathbf{R}(\psi)\,\mathbf{L}_{\delta,\vartheta}, \qquad \mathbf{L}_{\delta,\vartheta} = \begin{bmatrix} \cos\frac{\delta}{2} - j\sin\frac{\delta}{2}\cos 2\vartheta & -j\sin\frac{\delta}{2}\sin 2\vartheta \\ -j\sin\frac{\delta}{2}\sin 2\vartheta & \cos\frac{\delta}{2} + j\sin\frac{\delta}{2}\cos 2\vartheta \end{bmatrix}, \tag{13}$$

where ψ, δ, and ϑ denote the global rotation, retardance, and fast-axis orientation, respectively. Assigning $\mathbf{J}_{\text{tx}} = \mathbf{U}(\psi_t,\delta_t,\vartheta_t)$ and $\mathbf{J}_{\text{rx}} = \mathbf{U}(\psi_r,\delta_r,\vartheta_r)$ ensures $\mathbf{U}^\dagger\mathbf{U} = \mathbf{I}$.

Optimization. Given a set of measured Jones responses $\{\mathbf{J}^\star(\theta_n)\}_{n=1}^N$ acquired at different linear polarizer angles $\{\theta_n\}$, the decomposition problem is formulated as a constrained optimization:

$$\min_{\Theta} \sum_{n=1}^{N} \left\| \mathcal{M}\big(\mathbf{J}(\theta_n;\Theta)\big) - \mathcal{M}\big(\mathbf{J}^\star(\theta_n)\big) \right\|_F^2, \tag{14}$$

where $\mathcal{M}(\cdot)$ denotes the Jones-to-Mueller mapping [35] and $\Theta = \{\gamma, \psi_{t/r}, \delta_{t/r}, \vartheta_{t/r}, r_{1/2}, \phi_{1/2}, \alpha\}$ collects all unknowns.

We use the Jones-to-Mueller mapping to account for the global phase offsets present in our measured Jones matrices. In practice, each Jones response $\mathbf{J}^\star(\theta_n)$ is acquired at a different time and is therefore multiplied by an unknown global phase factor arising from interferometric phase drift between the local oscillator and signal, laser frequency noise, and path-length fluctuations [1]. However, the polarization state depends only on the relative phase between the orthogonal polarization channels. Consequently, measurement-to-measurement variations in this global phase offset can cause our optimization (Eq. (14)) to fail if we penalize discrepancies directly in the Jones matrix domain. In contrast, the corresponding Mueller matrices $\mathcal{M}(\mathbf{J})$ are invariant to global phase, and therefore keep the relative amplitudes and relative phase between the two orthogonal polarization components unchanged. Defining the loss in the Mueller domain therefore resolves the phase ambiguity. A derivation and illustrative example are provided in Supplement 1, Section 2.B.

5. Results

5.1. Hardware Prototype

As shown in Fig. 5, the experimental lidar prototype employs a Ciena WaveLogic 5n optical modem operating at a wavelength of 1550 nm. The modem samples the optical field at 74 GHz, yielding an optical depth resolution of 2 mm. The transmitted sequence length is constrained by the internal modem memory to approximately 2^{16} symbols, corresponding to an exposure time of 0.89 μs. Waveform programming and data acquisition are performed via the QSFP-DD electrical interface. An Erbium-doped fiber amplifier (Thorlabs EDFA300S) is incorporated in the transmitted path to increase the optical power. During operation, the average transmitted power is 2.1 mW, well below the Class 1 limit at 1550 nm (~10 mW, continuous wave). A second amplifier (Thorlabs EDFA100S) is deployed in the received path to pre-amplify the backscattered signal to roughly 0.9 mW, ensuring optimal input power for the modem. A Thorlabs CFS18-1550-APC fiber collimator lens converts the fiber output into a low-divergence free-space beam, maintaining beam quality across the working distance. The outgoing beam is deflected by a Thorlabs GVS012 dual-axis scanning galvanometer, enabling precise angular control for raster scanning and three-dimensional scene acquisition.

5.2. Experimental Results

5.2.1. Evaluation of Polarization–Depth–Velocity Reconstruction

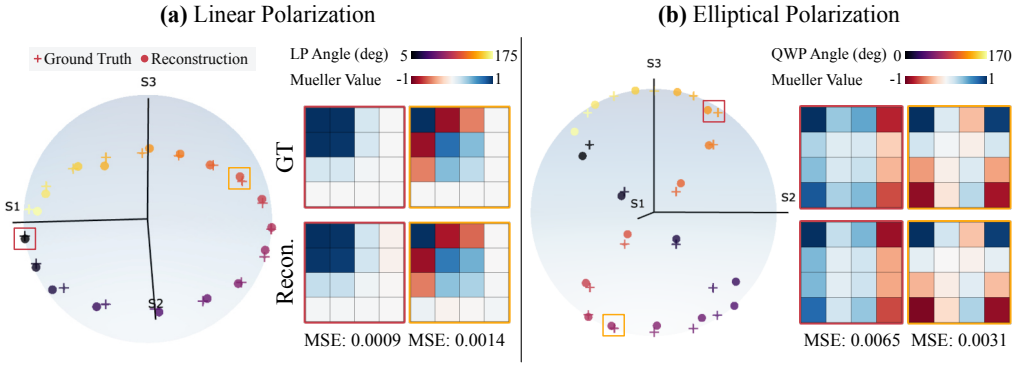

Fig. 6. **Polarization calibration results.** **(a)** We rotate the linear polarizer to generate a set of linearly polarized input states (Stokes vectors) and compare the ground truth (cross) with the reconstruction (dot) on the Poincaré sphere. Representative Mueller-matrix reconstructions for two of these states (red and yellow squares) are shown with their mean squared error (MSE). **(b)** We place a QWP after the linear polarizer and rotate the QWP to produce elliptical states; the recovered Stokes trajectory and two example Mueller matrices are shown in the same manner.

Polarization calibration evaluation. To evaluate polarization recovery accuracy, we perform two controlled tests: (1) a linear polarizer (LP) rotated to 18 angles from 5° to 175° (excluding calibration angles), and (2) a cascaded LP(0°) plus quarter-wave plate (QWP) with the QWP rotated from 0° to 170° in 18 steps. For each case, we convert the reconstructed Jones matrices to Stokes vectors and plot them on the Poincaré sphere (Fig. 6), comparing reconstructed states (dots) to analytical ground truth from ideal LP/QWP models (crosses). The recovered trajectories closely follow the theoretical loci for both linear and elliptical states. Fig. 6 also reports representative reconstructed Mueller matrices, showing close agreement with ground truth across all elements (MSE $\sim 10^{-3}$). A comparison with and without polarization calibration is also provided in Supplement 1, Section 5.A. We also evaluate the calibration efficiency and repeatability in Supplement 1, Section 2.C.

In addition to standard polarization elements, we compare the reconstructed Mueller matrix of a 3D object against physics-based polarimetric simulations [39] under matched configurations, which shows good qualitative agreement (details are provided in Supplement 1, Section 4).

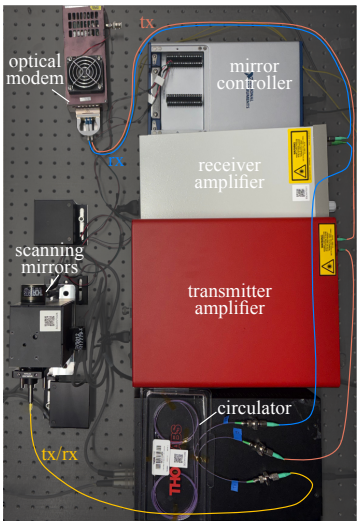

Fig. 5. **Hardware prototype.** The system consists of a coherent optical modem, transmitter and receiver EDFAs, a fiber circulator, scanning mirrors, and a controller.

Depth and velocity reconstruction across algorithms. We compare the proposed method with a matched-filter baseline and the FWL approach [30]. The matched filter fails to accurately recover depth for moving objects and cannot estimate radial velocity. Both FWL and our method jointly reconstruct depth and velocity; however, by explicitly accounting for incoherent power in a likelihood-based formulation, our method is more robust in low-SNR regions and achieves the lowest Mean Absolute Error (MAE) for both depth (4.37 mm) and radial velocity (0.86 m/s), as shown in Fig. 7. Additionally, we accelerate the forward model using FFT-based convolution,

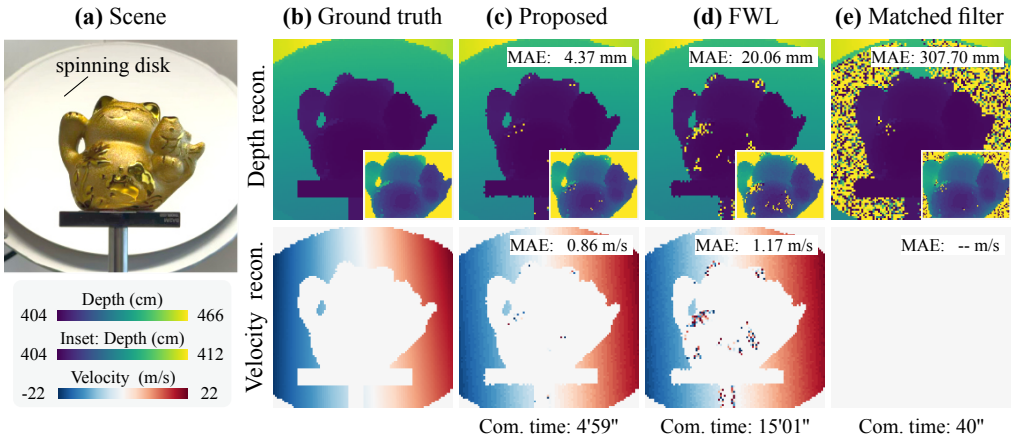

Fig. 7. **Comparison of depth and velocity reconstruction across algorithms. (a)** Experimental scene with a figurine and a spinning disk. **(b)** Ground-truth depth and radial velocity maps (depth from high-power acquisition; velocity from a high-speed camera, see details in Supplement 1, Section 5.B). **(c–e)** Reconstructed depth (top) and radial velocity (bottom) using the proposed method, FWL [30], and a matched-filter baseline. MAE and computation time are reported in each column. The matched-filter baseline cannot estimate radial velocity.

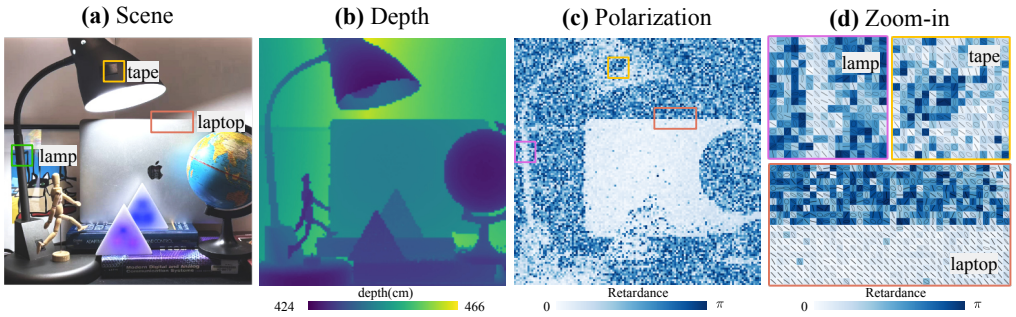

Fig. 8. **Reconstruction under strong ambient light. (a)** A tabletop scene is lit by multiple uncontrolled sources (desk lamp, ceiling light, triangular-shaped blue and purple LEDs), creating strong spatially-varying background light. **(b)** Despite the presence of ambient light, coherent detection enables robust depth recovery with clear object geometry. **(c)** The reconstructed polarimetric response remains accurate under ambient illumination. **(d)** The zoomed-in insets reveal metallic–dielectric differences in both retardance and the overlaid Jones ellipse features (orientation and ellipticity), comparing the lamp arm/head and laptop with the background paper and tape.

making our implementation approximately three times faster than FWL. All computation times are reported as wall-clock time measured on an Intel Xeon Gold 5120 CPU and an NVIDIA TITAN RTX GPU. Additional analyses are provided in Supplement 1, Section 5.B. We further evaluate reconstruction performance over varying target depths, target velocities, and SNR levels in Supplement 1, Section 5.C.

5.2.2. Reconstruction under Ambient Light

To demonstrate robustness under realistic, uncontrolled indoor lighting conditions, we capture scenes in a brightly lit indoor environment (about 10^4 lux), under simultaneous illumination from

desk lamps, ceiling lights, triangular-shaped blue and purple LEDs (Fig. 8(a)).

Despite the strong illumination, our coherent polarimetric pipeline still jointly reconstructs accurate depth and polarization information. Fig. 8(b) shows that the recovered depth preserves the scene geometry, while the reconstructed Jones retardance map in Fig. 8(c) remains well-structured and retains material-discriminative signatures. The zoom-ins in Fig. 8(d) highlight three representative regions: (1) the lamp arm against the picture-frame background, (2) the lamp head with an attached tape patch, and (3) the laptop surface against a paper background. Across these examples, metallic regions (lamp and laptop) appear spatially smooth, with locally correlated retardance and consistent Jones-ellipse orientation and ellipticity, whereas the dielectric regions (tape and background) exhibit noticeably higher spatial variability with patchier, speckle-like fluctuations in both retardance and the recovered Jones-ellipse patterns.

5.2.3. Polarization Coherent Speckle Reconstruction Results

Polarization speckle reconstruction for different materials. As shown in Fig. 9(a–b), we investigate the polarization-coherent speckle characteristics across different materials: a painted metallic car body panel, a translucent wax block, a 3D-printed polymer figurine (PLA), an artificial (plastic) plant, and a real plant leaf. For each target we scan a 2 mm by 2 mm patch and reconstruct both the intensity speckle and the associated polarization field (Stokes vectors and SDoP). Fig. 9(c) compares the reconstructed intensity speckle overlaid with polarization speckle for all materials. While the intensity speckle patterns appear random and visually similar, their polarization structures are markedly different.

For metallic surfaces, their large imaginary refractive index confines light within a shallow skin depth and maintains a nearly constant phase relationship between the two orthogonal polarized components, resulting in spatially coherent polarization states with the highest SDoP. Dielectric 3D-printed surfaces exhibit stronger polarization mixing and angle-dependent Fresnel effects, producing lower SDoP and more rapidly varying polarization speckle. Translucent wax shows intermediate behavior: subsurface scattering reduces SDoP relative to metal but still preserves smoother polarization structures than the rough dielectric. Finally, the real plant leaf exhibits strongly randomized polarization with low SDoP due to multiple volume-scattering layers, whereas the artificial plant—made of smooth polymer—produces polarization speckle patterns similar to the 3D-printed object. These observations demonstrate that polarization-coherent speckle encodes rich, material-dependent scattering signatures that are not discernible from intensity-only measurements.

Effect of varying surface roughness on polarization speckle. As described by the polarization speckle model in Sec. 2.2, surface height variations modulate the optical path length and introduce a spatially-varying phase term. As the variance of surface height increases, the path length fluctuations decorrelate the field between neighboring micro-facets, reducing the local SDoP and making the polarization speckle more random.

To experimentally verify this relationship, we measure polarization speckle on a set of sandpaper samples with calibrated roughness levels (70–270 μm grain size). For each sample, we reconstruct the polarization-resolved Jones matrix field over a 2 mm by 2 mm patch and visualize the resulting polarization speckle, together with the corresponding SDoP. As shown in Fig. 9(c), as the surface roughness increases (corresponding to a larger grain size), SDoP decreases monotonically, indicating stronger depolarization and higher speckle randomness.

We further investigate these trends in Supplement 1, Section 3, where we analyze how polarization speckle statistics and SDoP vary with the system aperture size and scanned field-of-view. These results show that larger apertures and wider scan areas encompass more independent scatterers, which strengthens speckle randomness and further reduces the measured SDoP.

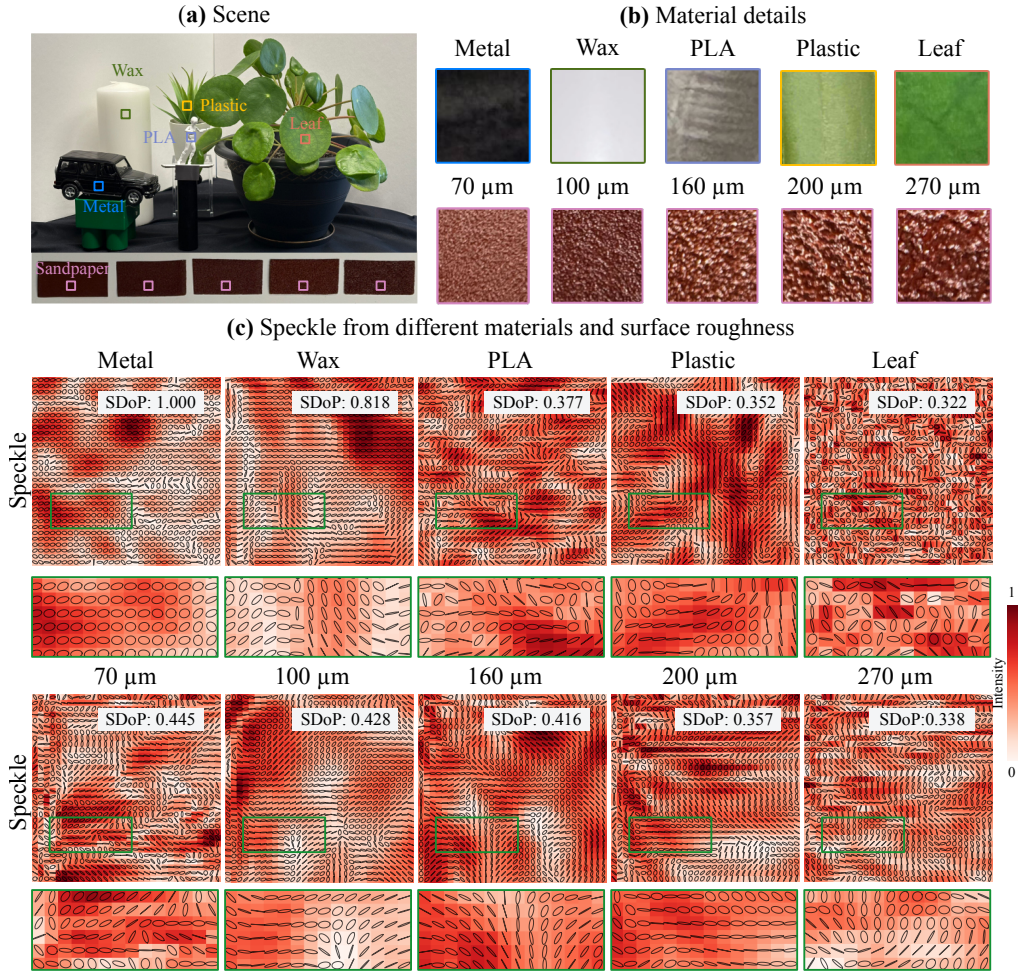

Fig. 9. **Polarization speckle from different materials and surface roughness. (a–b)** Test scene and surface details for five representative materials (metal, wax, PLA, plastic, and leaf) together with sandpaper samples of increasing grain size (70–270 μm). **(c)** For each material and sandpaper sample, we visualize the reconstructed intensity speckle overlaid with polarization ellipses over an approximately 2 mm by 2 mm scan, along with a zoomed-in patch. The SDoP decreases from metal to translucent wax and dielectric PLA/plastic due to increasing subsurface scattering that progressively randomizes polarization. The real leaf, dominated by multiple scattering within complex biological microstructures, exhibits highly random polarization states. For sandpaper, the SDoP decreases monotonically as the surface becomes rougher.

5.2.4. Polarimetric Imaging Through Scattering Media

Polarimetric information can provide material-sensitive contrast in imaging-through-scattering settings where intensity contrast is weak. To evaluate this capability, we image a metallic plate carrying a dielectric "T" target through two scattering media: thin diffuser layers with varying grit levels (Thorlabs DG20-1500, DG10-600, DG20-220, and DG10-120) and thicker semi-translucent polymethyl methacrylate (PMMA) acrylic slabs with varying thicknesses (1, 1.5, 2, and 3 mm). Scattering strength is quantified by transmittance, and additionally by optical thickness (OT) for PMMA slabs. Fig. 10 presents the weakest and strongest scattering endpoints

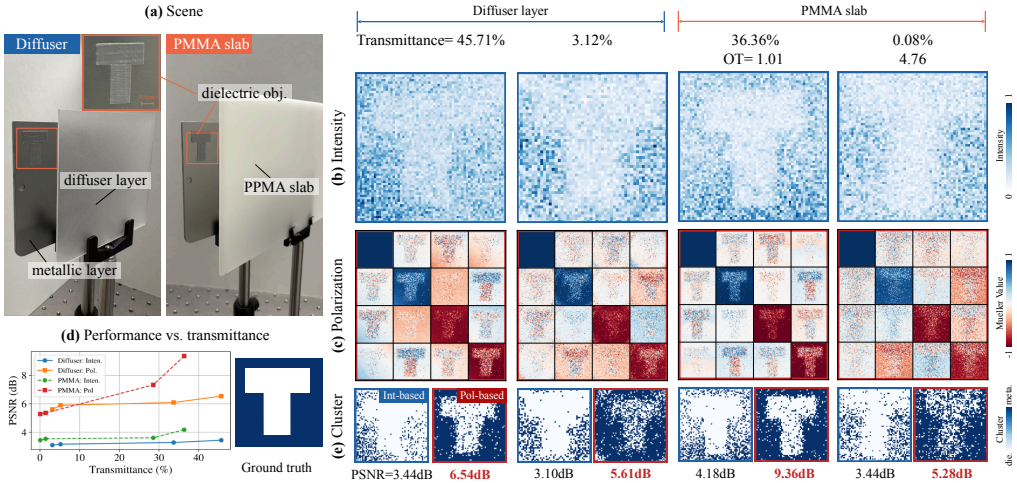

Fig. 10. **Polarimetric imaging through scattering media with varying scattering strength.** **(a)** A dielectric "T" target is attached to a metallic plate and imaged through either thin diffuser layers or semi-translucent PMMA acrylic slabs. **(b)** Intensity reconstructions under representative weak and strong scattering conditions: diffuser layers with transmittance of 45.71% and 3.12%, and PMMA slabs with transmittance of 36.36% and 0.08%, corresponding to OT of 1.01 and 4.76. **(c)** Reconstructed Mueller-matrix responses, which preserve material-dependent contrast between the metallic background and dielectric target. **(d)** Quantitative material-recovery performance versus transmittance, with PSNR computed against the binary "T" ground-truth mask. **(e)** Material clustering results using intensity-based and polarization-based features. Polarization-based clustering consistently improves dielectric–metallic separation, while performance degrades as scattering becomes stronger.

from each medium, with the complete sweep over all conditions provided in Supplement 1, Section 5.D. Because the experiment is performed in a reflective imaging-through-scattering geometry, the light traverses the scattering medium twice, making the reconstruction more challenging. Under these conditions, the intensity reconstructions provide weak material contrast because the dielectric target and metallic background have similar albedo and the scattering medium further blurs the coherent speckle (Fig. 10(b)). In contrast, the reconstructed Mueller responses retain clearer dielectric–metallic differences (Fig. 10(c)).

We evaluate material recovery by applying the same two-component clustering model [40] to either intensity features or Mueller-matrix features. The resulting segmentation is compared against a binary "T" mask obtained from a reference scan without the scattering medium. Across both diffuser and PMMA conditions, polarization-based clustering outperforms intensity-based clustering, while the advantage decreases as scattering becomes stronger (Fig. 10(d–e)).

6. Conclusion

Our work repurposes a compact telecommunications-grade optical modem for polarimetric full-wavefield coherent lidar. We introduce a polarimetric image formation model and reconstruction framework, and show that from a single coherent measurement per point we can recover not only depth and velocity but also an effective surface backscattering Jones response observed through the system's illumination and collection aperture. By using our system to scan an entire scene, we can also perform spatial polarization analysis based on polarization speckle statistics, which goes beyond what conventional intensity-only or conventional coherent lidar systems can measure. Finally, our work shows the compatibility of telecommunications technology with coherent lidar.

Our investigation opens several directions for future work. Coherent speckle still limits the fidelity of the recovered Jones matrices, and the scanning-based acquisition process remains time-consuming (see Supplement 1, Section 5.F). Addressing these issues—e.g., by incorporating speckle denoising, learning-based priors, and real-time processing—could improve reconstruction fidelity and reduce latency. We hope that our work spurs further investigation into compact, low-cost, polarization-resolved coherent lidar systems and algorithms that leverage off-the-shelf photonic components. More broadly, advances in this area could enable new forms of lidar and multimodal perception, improving sensing in low-visibility conditions for autonomous driving and remote sensing.

Acknowledgment. We thank Ciena Corporation for loaning the optical modem. DBL and KNK acknowledge support from Ciena Corporation, the Canada Foundation for Innovation, the Ontario Research Fund, and NSERC under the RGPIN, and Alliance programs. DD was supported by the Faculty of Arts & Science Postdoctoral Fellowship Award. PM was supported by the Mitacs Accelerate program. SB was partly supported by the National Research Foundation of Korea (NRF) (No. RS-2024-00438532 and No. RS-2023-00211658), the Institute of Information & Communications Technology Planning & Evaluation (IITP) grant (No. RS-2024-0045788), and the IITP-ITRC (Information Technology Research Center) grant (IITP-2026-RS-2024-00437866), all funded by the Korea government (MSIT).

Disclosures. The authors declare no conflicts of interest.

Supplemental document. See Supplement 1 for supporting content.

References

1. K. Kikuchi, "Fundamentals of coherent optical fiber communications," J. Light. Technol. **34**, 157–179 (2015).
2. S. Gao, M. O'Sullivan, and R. Hui, "Complex-optical-field LiDAR system for range and vector velocity measurement," Opt. Express **20**, 25867–25875 (2012).
3. S. W. Henderson, P. Gatt, D. Rees, and R. M. Huffaker, "Wind LiDAR," in *Laser Remote Sensing,* (2005), pp. 487–740.
4. T. Wei, H. Xia, B. Yue, *et al.*, "Remote sensing of raindrop size distribution using the coherent Doppler LiDAR," Opt. Express **29**, 17246–17257 (2021).
5. Y. Li and J. Ibanez-Guzman, "LiDAR for autonomous driving: The principles, challenges, and trends for automotive LiDAR and perception systems," IEEE Signal Process. Mag. **37**, 50–61 (2020).
6. C. V. Poulton, M. J. Byrd, P. Russo, *et al.*, "Long-range LiDAR and free-space data communication with high-performance optical phased arrays," IEEE J. Sel. Top. Quantum Electron. **25**, 1–8 (2019).
7. D. H. Goldstein, *Polarized Light* (CRC Press, 2017).
8. J. W. Goodman, *Speckle Phenomena in Optics: Theory and Applications* (Roberts and Company Publishers, 2007).
9. J. R. Serres, P.-J. Lapray, S. Viollet, *et al.*, "Passive polarized vision for autonomous vehicles: A review," Sensors **24**, 3312 (2024).
10. R. Blin, S. Ainouz, S. Canu, and F. Meriaudeau, "Road scenes analysis in adverse weather conditions by polarization-encoded images and adapted deep learning," in *Proc. IEEE Intell. Transp. Syst. Conf. (ITSC),* (2019), pp. 27–32.
11. Z. Zhu, X. Li, J. Zhai, and H. Hu, "PODB: A learning-based polarimetric object detection benchmark for road scenes in adverse weather conditions," Inf. Fusion **108**, 102385 (2024).
12. C. Taglione, J. Guzzi, B. Cannelle, and D. Floreano, "Polarimetric imaging for robot perception: A review," Sensors **24**, 4440 (2024).
13. A. Kalra, V. Taamazyan, S. K. Rao, *et al.*, "Deep polarization cues for transparent object segmentation," in *Proc. IEEE/CVF Conf. Comput. Vis. Pattern Recognit.*, (2020), pp. 8602–8611.
14. J. Jiang, G. Cao, J. Deng, *et al.*, "Robotic perception of transparent objects: A review," IEEE Trans. Artif. Intell. **5**, 2547–2567 (2024).
15. O. Morel and P. Gorria, "Polarization imaging for 3d inspection of highly reflective metallic objects," Opt. Spectrosc. **101**, 11–17 (2006).
16. F. Meriaudeau, M. Ferraton, C. Stolz, *et al.*, "Polarization imaging for industrial inspection," in *Proc. SPIE Image Process. Mach. Vis. Appl.*, vol. 6813 (SPIE, 2008), p. 681308.
17. Q. Liu, S. Wu, B. Liu, *et al.*, "Shipborne variable-fov, dual-wavelength, polarized ocean LiDAR: Design and measurements in the Western Pacific," Opt. Express **30**, 8927–8948 (2022).
18. A. P. Vasilkov, Y. A. Goldin, B. A. Gureev, *et al.*, "Airborne polarized LiDAR detection of scattering layers in the ocean," Appl. Opt. **40**, 4353–4364 (2001).
19. X. Liu, L. Zhang, X. Zhai, *et al.*, "Polarization LiDAR: Principles and applications," Photonics **10**, 1118 (2023).
20. M. Amani, A. Moghimi, S. M. Mirmazloumi, *et al.*, "Ocean remote sensing techniques and applications: A review (part i)," Water **14**, 3400 (2022).
21. J. Zheng, *Optical Frequency-Modulated Continuous-Wave (FMCW) Interferometry* (Springer, 2005).

22. S. Gao and R. Hui, "Frequency-modulated continuous-wave LiDAR using I/Q modulator for simplified heterodyne detection," Opt. Lett. **37**, 2022–2024 (2012).
23. L. Zhang, J. Sun, H. Cong, *et al.*, "Polarimetric imaging LiDAR based on FMCW and Mueller matrix for target classification," J. Light. Technol. (2024).
24. N. Takeuchi, H. Baba, K. Sakurai, and T. Ueno, "Diode-laser random-modulation CW LiDAR," Appl. Opt. **25**, 63–67 (1986).
25. C. S. Sambridge, J. T. Spollard, A. J. Sutton, *et al.*, "Detection statistics for coherent RMCW LiDAR," Opt. Express **29**, 25945–25959 (2021).
26. A. Lukashchuk, J. Riemensberger, A. Tusnin, *et al.*, "Chaotic microcomb-based parallel ranging," Nat. Photonics **17**, 814–821 (2023).
27. P. Tang, M. A. Kirby, N. Le, *et al.*, "Polarization-sensitive optical coherence tomography with single input for imaging depth-resolved collagen organizations," Light Sci. Appl. **10**, 237 (2021).
28. J. F. De Boer, C. K. Hitzenberger, and Y. Yasuno, "Polarization-sensitive optical coherence tomography—a review," Biomed. Opt. Express **8**, 1838–1873 (2017).
29. Y. Sun, J. Wang, J. Shi, and S. A. Boppart, "Synthetic polarization-sensitive optical coherence tomography by deep learning," NPJ Digit. Med. **4**, 105 (2021).
30. P. Mirdehghan, B. Buscaino, M. Wu, *et al.*, "Coherent optical modems for full-wavefield LiDAR," in *Proc. SIGGRAPH Asia,* (2024).
31. E. Ip, A. P. T. Lau, D. J. F. Barros, and J. M. Kahn, "Coherent detection in optical fiber systems," Opt. Express **16**, 753–791 (2008).
32. B. E. A. Saleh and M. C. Teich, *Fundamentals of Photonics, 2-Volume Set* (John Wiley & Sons, 2019).
33. A. Yariv and P. Yeh, *Photonics: Optical Electronics in Modern Communications*, vol. 6 (Oxford University Press, 2007).
34. G. P. Agrawal, *Fiber-Optic Communication Systems* (John Wiley & Sons, 2012).
35. R. Chipman, W. S. T. Lam, and G. Young, *Polarized Light and Optical Systems* (CRC Press, 2018).
36. M. Takeda, W. Wang, and S. G. Hanson, "Polarization speckles and generalized stokes vector wave: a review," in *Proc. SPIE Speckle: Int. Conf. Speckle Metrol.*, vol. 7387 (2010), pp. 257–263.
37. R. C. Jones, "A new calculus for the treatment of optical systems. i. description and discussion of the calculus," J. Opt. Soc. Am. **31**, 488–493 (1941).
38. S. T. Tang and H. S. Kwok, "3 × 3 matrix for unitary optical systems," J. Opt. Soc. Am. A **18**, 2138–2145 (2001).
39. S.-H. Baek and F. Heide, "All-photon polarimetric time-of-flight imaging," in *Proc. IEEE/CVF Conf. Comput. Vis. Pattern Recognit.*, (2022), pp. 17876–17885.
40. C. M. Bishop, *Pattern Recognition and Machine Learning* (Springer, 2006).